



# The effect of sintering temperature and time on the growth of single crystals of $0.75 (\text{Na}_{0.5}\text{Bi}_{0.5})\text{TiO}_3\text{--}0.25 \text{SrTiO}_3$ by solid state crystal growth

Phan Gia Le<sup>1</sup> · Gi-Young Jo<sup>2</sup> · Seok-Young Ko<sup>2,3</sup> · John G. Fisher<sup>1</sup>

Received: 10 January 2017 / Accepted: 2 January 2018 / Published online: 12 January 2018  
© Springer Science+Business Media, LLC, part of Springer Nature 2018

## Abstract

Materials in the  $(\text{Na}_{0.5}\text{Bi}_{0.5})\text{TiO}_3\text{--SrTiO}_3$  system are of interest for use as lead-free piezoelectric actuators due to high electric-field induced strains. Piezoelectric properties may be further improved by growing single crystals but as yet work on single crystal growth in this system is limited. In the present work, single crystals of composition  $0.75 (\text{Na}_{0.5}\text{Bi}_{0.5})\text{TiO}_3\text{--}0.25 \text{SrTiO}_3$  were grown by solid state crystal growth (SSCG) on [001]  $\text{SrTiO}_3$  seed crystals and the dependence of crystal growth distance and matrix grain growth on sintering temperature investigated. Electron backscattered diffraction and X-ray diffraction analysis show that the single crystals grow epitaxially on the seed crystals. Energy dispersive spectroscopy indicates that the grown crystals are slightly Na-deficient, while X-ray photoelectron spectroscopy indicates the presence of oxygen vacancies. Single crystal growth distance, mean matrix grain size and grain size distribution as a function of sintering temperature and time are presented. Increasing the sintering temperature increases both single crystal and matrix grain growth rates. The optimum single crystal growth temperature is found to be  $1250^\circ\text{C}$ . The effect of sintering temperature on the single crystal and matrix grain growth behavior is explained using the mixed control mechanism of microstructural evolution.

**Keywords**  $(\text{Na}_{0.5}\text{Bi}_{0.5})\text{TiO}_3$  · Single crystal growth · Microstructure · Scanning electron microscopy · Abnormal grain growth

## 1 Introduction

Piezoelectric materials based on  $\text{Pb}(\text{Zr},\text{Ti})\text{O}_3$  (PZT) are widely applied in many electronic devices such as generators, actuators, transducers and motors [1, 2]. However, legislation restricting the use of lead by the European Union (EU), the United States and several other countries has prompted a search for lead-free piezoelectric materials to replace PZT. Many lead-free piezoelectric systems are being explored and developed based on barium titanate  $\text{BaTiO}_3$ , sodium bismuth titanate  $(\text{Na}_{0.5}\text{Bi}_{0.5})\text{TiO}_3$  (NBT) and potassium sodium niobate  $(\text{K}_{0.5}\text{Na}_{0.5})\text{NbO}_3$  (KNN) [1, 3]. Recent developments in this area

include the development of NBT-based incipient ferroelectric materials with large electric-field-induced strains [4–6], materials with core/shell microstructures [7, 8], textured ceramics [9, 10], materials with high electrostrictive strains [9, 11] and KNN-based materials with a rhombohedral-tetragonal polymorphic phase transition close to room temperature [12, 13]. In addition to their use as piezoelectric materials, materials from these systems also have applications in multiferroic composites [14, 15] electrocaloric devices [16, 17] and energy storage devices [18, 19].

In 1961, Smolenskii et al. [20] found NBT to be a perovskite-type ferroelectric material at room temperature. NBT is a relaxor ferroelectric which undergoes a phase transition between rhombohedral and tetragonal phases between  $200$  and  $320^\circ\text{C}$  ( $T_{\text{R-T}}$ ) and between tetragonal and cubic phases at  $\sim 540^\circ\text{C}$  [1, 21–24]. In addition, there is a depolarization temperature  $T_d$  at  $\sim 185^\circ\text{C}$  [25]. This is generally considered to be a ferroelectric-antiferroelectric transition [26] but its exact nature is still disputed, having also been described as a weakening of the ferroelectric domains associated with a reduction of octahedral tilting [27].  $T_d$  and  $T_{\text{R-T}}$  may also be lowered and even merged together when NBT forms a solid solution with another component [28, 29]. NBT possesses a large remnant polarization ( $P_r = 38 \mu\text{C}/\text{cm}^2$ ), high coercivity

✉ John G. Fisher  
johnfisher@jnu.ac.kr

<sup>1</sup> School of Materials Science and Engineering, Chonnam National University, 77 Yongbong-ro, Buk-gu, Gwangju 61186, Republic of Korea

<sup>2</sup> Department of Materials Science and Engineering, Korea Advanced Institute of Science and Technology (KAIST), 291 Daehak-ro, Yuseong-gu, Daejeon 34141, Republic of Korea

<sup>3</sup> Present address: Agency for Defense Development, P.O. Box 35, Yuseong, Daejeon 34186, Republic of Korea

( $E_c = 70 \text{ kV cm}^{-1}$ ) and high temperature of maximum permittivity ( $T_m = 320^\circ\text{C}$ ) [1, 22, 30]. Many NBT-based binary and ternary systems have been constructed to improve NBT's piezoelectric properties [1, 3, 31, 32]. NBT-based solid solutions exhibit high strains due to a reversible electric field induced phase transformation between relaxor and ferroelectric phases, which makes them attractive for actuator applications [4–6, 31, 32]. However, these materials have several problems: the necessity of a large driving field to induce the phase transition, high strain hysteresis and temperature sensitivity of properties [9]. SrTiO<sub>3</sub> (ST) addition to NBT to make  $(1-x)\text{NBT} - x\text{ST}$  (NBT-ST) solid solutions has been reported [33, 34]. The addition of ST into NBT slightly increases the tolerance factor of NBT-ST solid solutions because the tolerance factor of 1.013 for ST is larger than the tolerance factor of 0.977 for NBT [35]. This indicates that the NBT-ST rhombohedral structure is altered to a more symmetric cubic structure as ST concentration increases, so that the NBT-ST structure changes from the rhombohedral to cubic phase [35, 36]. When  $x \approx 0.25$ , a morphotropic phase boundary (MPB) exists between rhombohedral and pseudocubic phases and  $T_d$  and  $T_{R-T}$  are lowered to room temperature [33, 35, 37]. Compositions around this MPB were reported to have excellent converse piezoelectric properties (e.g.  $d_{33}^* \approx 600 \text{ pm/V}$  at an electric field of 4 kV/mm for the 0.75 (Na<sub>0.5</sub>Bi<sub>0.5</sub>)TiO<sub>3</sub>–0.25 SrTiO<sub>3</sub> composition) [33, 38]. This combination of high  $d_{33}^*$  and relatively low driving field makes these materials attractive for actuator applications. The driving field can be lowered further by acceptor doping [39].

NBT-based ceramics have a polycrystalline structure with randomly oriented grains. This reduces the degree of domain orientation in an electric field, leading to significantly decreased piezoelectric properties. The piezoelectric properties of NBT-based materials can be improved through fabrication of single crystals [40, 41]. There are many techniques to grow single crystals such as self-flux, Bridgman and top seeded single crystal growth [42, 43], but these methods required the starting materials to be heated up until they are molten. This can lead to chemical inhomogeneity within the single crystals due to the evaporation of low melting temperature materials and incongruent melting [44, 45]. An alternative method of growing single crystal is via the solid state single crystal growth (SSCG) technique [44, 46, 47]. In this technique, a single crystal (called a seed crystal) is buried within ceramic powder, pressed into a pellet and then sintered. During sintering, a single crystal of the ceramic composition grows on the seed crystal. The SSCG technique takes place under normal ceramic sintering temperatures, removing the need to melt the starting materials, and uses inexpensive crucibles and furnaces [47]. In addition, the SSCG method does not suffer from contamination from Pt crucibles and can grow single crystals of specific orientation. Thus, SSCG was employed to grow single crystals of KNN [44, 48], KNN-ST [49, 50], NBT-

BaTiO<sub>3</sub> (BT) [46], NBT-20ST [51] and NBT – Ba(Zr,Ti)O<sub>3</sub> [52]. Single crystals of NBT-BT-KNN and NBT-CaTiO<sub>3</sub> were recently grown by SSCG and were found to have superior converse piezoelectric properties to their polycrystalline equivalents [40, 53, 54]. Therefore it is possible that the piezoelectric properties of NBT-ST materials could be improved further by preparing them in single crystalline form.

In the present work, 75 mol% (Na<sub>0.5</sub>Bi<sub>0.5</sub>)TiO<sub>3</sub>–25 mol% SrTiO<sub>3</sub> (NBT-25ST) single crystals were grown by the SSCG method. This particular composition was chosen due to the excellent piezoelectric properties reported for polycrystalline ceramics [8, 38, 55]. The SSCG method is a type of induced abnormal grain growth (AGG). The seed crystal acts as an abnormal grain which grows more rapidly than the surrounding matrix grains to form the single crystal [47]. AGG behavior has been explained using the mixed control mechanism of microstructural evolution [47, 56, 57]. According to this mechanism, the sintering temperature is expected to greatly affect the single crystal growth behavior due to its effect on the critical driving force for abnormal grain growth and grain boundary diffusion; however this has not been studied in previous works on NBT-based systems [46, 52]. The effect of sintering temperature on matrix grain growth behavior is also important, as matrix grain size controls the driving force for single crystal growth. Hence, the effect of sintering temperature on single crystal and matrix grain growth was studied in the present work in order to find the optimum sintering temperature for NBT-25ST.

## 2 Experimental

The 75 mol% (Na<sub>0.5</sub>Bi<sub>0.5</sub>)TiO<sub>3</sub>–25 mol% SrTiO<sub>3</sub> powder is synthesized from Na<sub>2</sub>CO<sub>3</sub> (ACROS organics, 99.5%), Bi<sub>2</sub>O<sub>3</sub> (Alfa Aesar, 99.9%), TiO<sub>2</sub> (Alfa Aesar, 99.8%) and SrCO<sub>3</sub> (Aldrich,  $\geq 99.9\%$ ) starting materials by solid state reaction. The starting materials are dried in an oven at 250°C for 5 h to remove absorbed water. The stoichiometrically weighed amounts of these starting materials are mixed and ground in high-purity (99.9%) ethanol in a ZrO<sub>2</sub>-lined jar in a planetary ball mill (Planetary Micro Mill Pulverisette 7, Fritsch GmbH, Idar-Oberstein, Germany) for 3 h (alternating 5 min milling and rest periods) at 500 rpm using ZrO<sub>2</sub> media. After milling, the ethanol is evaporated using a hot plate / magnetic stirrer. Then, the slurry is dried in an oven at 80°C for 12 h to totally remove any remaining ethanol. The dried slurry is ground in an agate mortar and pestle and sieved through a 180  $\mu\text{m}$  sieve to remove agglomerates. The powder is put into high purity alumina double crucibles with lids and calcined at 850°C for 3 h in air, with heating and cooling rates of 5°C/min. The calcined powder is planetary ball milled, ground and sieved again to reduce the particle size. The powder is analyzed by X-ray diffraction (XRD, X'Pert PRO, PANalytical, Almelo, the

Netherlands) using Cu K $\alpha$  radiation with a scan range of 20–90° 2 $\theta$ , a step size of 0.02° and a scan rate of 3°/min. Particle size analysis of the powder was carried out using a zeta potential/particle size analyzer (ELS-8000, Otsuka Electronics, Osaka, Japan).

SrTiO<sub>3</sub> single crystal seeds (MTI Corp., CA) with [001] orientation and dimensions of 5 × 5 × 0.5 mm are buried in the powder in a 10 mm steel die and pressed by hand into pellets. Then the pellets are pressed in a cold isostatic press (CIP) at 1500 kg/cm<sup>2</sup> (~ 147 MPa). The CIPed pellets are buried inside packing powder of the same composition in high purity alumina double crucibles with lids and sintered at 1100, 1150, 1200 and 1250°C for 1, 5, 10, 20 and 50 h with heating and cooling rates of 5°C/min. The samples are vertically sectioned using a low speed diamond wheel saw, polished to a 1  $\mu$ m finish and thermally etched. The etched samples are Pt-coated and observed by scanning electron microscopy (SEM, Hitachi S-4700, Tokyo, Japan) with attached energy dispersive X-ray spectrometer (EDS, EMAX energy EX-200, Horiba, Kyoto, Japan). The single crystal growth distance, mean matrix grain size and matrix grain size distribution are analyzed from the SEM micrographs using imageJ v1.50a image analysis software. To analyze single crystal thickness, the single crystal in each micrograph is divided into slices and the area of each slice measured. By dividing the area of each slice by its width, the average growth distance of the crystal in that slice could be measured. For each sample, the mean and standard deviation of 50 slices are measured. To analyze the mean matrix grain size and grain size distribution, the equivalent 2D radii of at least 200 grains are analyzed for each sample.

One sample sintered at 1250°C for 5 h is prepared for electron backscattered diffraction analysis (EBSD). The sample is vertically sectioned as before and polished to a 0.25  $\mu$ m finish, but not thermally etched. The sample is analyzed in a Quanta 3D FEG SEM (FEI, Hillsboro, OR) with a Hikari EBSD camera (EDAX, Mahwah, NJ). To carry out X-ray diffraction of a single crystal, a sample is sintered at 1250°C for 5 h and then ground and polished in the horizontal plane to a 1  $\mu$ m finish to expose the grown single crystal on one face. The sample is then examined using XRD as before. To carry out chemical analysis of the samples, samples are sintered at 1100, 1150, 1200 and 1250°C for 10 h and then ground and polished in the horizontal plane to a 1  $\mu$ m finish to expose the grown single crystal on one face. Samples are Pt coated and examined using EDS (EMAX energy EX-200, Horiba, Kyoto, Japan). For each sample, five points on the single crystal and five points on the matrix grains are examined. One sample sintered at 1200°C for 10 h is prepared for X-ray photoelectron spectroscopy with a monochromatic Al K $\alpha$  X-ray source (XPS, VG Multilab 2000, Thermo Scientific, UK). The sample is ground and polished in the horizontal plane to a 1  $\mu$ m finish. Before analysis, the sample surface is cleaned for 10 min using an Ar<sup>+</sup> ion beam to remove surface contamination.

For backscattered electron imaging, samples are vertically sectioned as before and polished to a 1  $\mu$ m finish but not thermally etched. Samples are Pt-coated and observed in a JSM-7500F SEM (JEOL, Tokyo, Japan) with attached energy dispersive X-ray spectrometer (Oxford Instruments, Abingdon, United Kingdom). To observe the surface morphology of the matrix grains, samples of NBT-25ST powder are annealed in an alumina crucible with lid in air at different temperatures for 10 h and then quenched by removing the crucible from the furnace and cooling in air. The quenched powder samples are then examined by SEM (Hitachi S-4700, Tokyo, Japan). To observe the matrix grain boundaries and triple junctions in more detail, ceramic samples (without seed crystals) are sintered at 1100 and 1150°C for 1 h. TEM samples are prepared by Focused Ion Beam (Helios NanoLab, FEI, the Netherlands) and viewed in a JEM-2100F (HR) microscope (JEOL, Tokyo, Japan) with Energy Dispersive Spectroscopy (EDS, Oxford Instruments, Abingdon, United Kingdom) using an accelerating voltage of 200 kV.

### 3 Results

An XRD pattern of the calcined NBT-25ST powder is shown in Fig. 1(a). The calcined powder has the perovskite structure and the XRD pattern could be indexed with PDF#89–3109 for (Na<sub>0.5</sub>Bi<sub>0.5</sub>)TiO<sub>3</sub> (cubic, space group *Pm-3m*). No secondary phases are present. The unit cell parameter for the calcined powder was calculated using the least-squares method (MDI Jade 6, Materials Data, Livermore CA). The unit cell parameter for the NBT-25ST powder is  $a = 3.90083 \pm 0.000615$  Å. This is slightly larger than the unit cell parameter for cubic NBT ( $a = 3.89$  Å). The ionic crystal radii of Na<sup>+</sup> and Sr<sup>2+</sup> in 12-fold coordination are 1.39 and 1.44 Å respectively [58]. The ionic radius of Bi<sup>3+</sup> in 12-fold coordination is not given, but the ionic radii of Bi<sup>3+</sup> and Sr<sup>2+</sup> in six-fold coordination are 1.03 and 1.18 Å respectively. Replacement of some of the Na<sup>+</sup> and Bi<sup>3+</sup> ions with the larger Sr<sup>2+</sup> ions causes an expansion in the unit cell. The particle size distribution of the NBT-25ST powder after calcination and ball milling shows a single peak which tails out to a maximum size of 850 nm [Fig. 1(b)]. The mean particle size is  $404 \pm 86$  nm.

SEM micrographs of NBT-25ST single crystals grown at 1200°C for 1–50 h are shown in Fig. 2. Single crystals of NBT-25ST have grown on the [001]-oriented SrTiO<sub>3</sub> seed crystals. The white dashed lines mark the boundaries between the seed crystal/single crystal and the single crystal/matrix grains. Both single crystal growth distance and matrix grain size increase with sintering time. The single crystals contain porosity, as do the matrix grains. The matrix grains contain a secondary phase. EDS shows this phase to contain mostly Ti and O, with some Na and a small amount of Sr. In some of the samples, the seed crystal also appears to contain a secondary

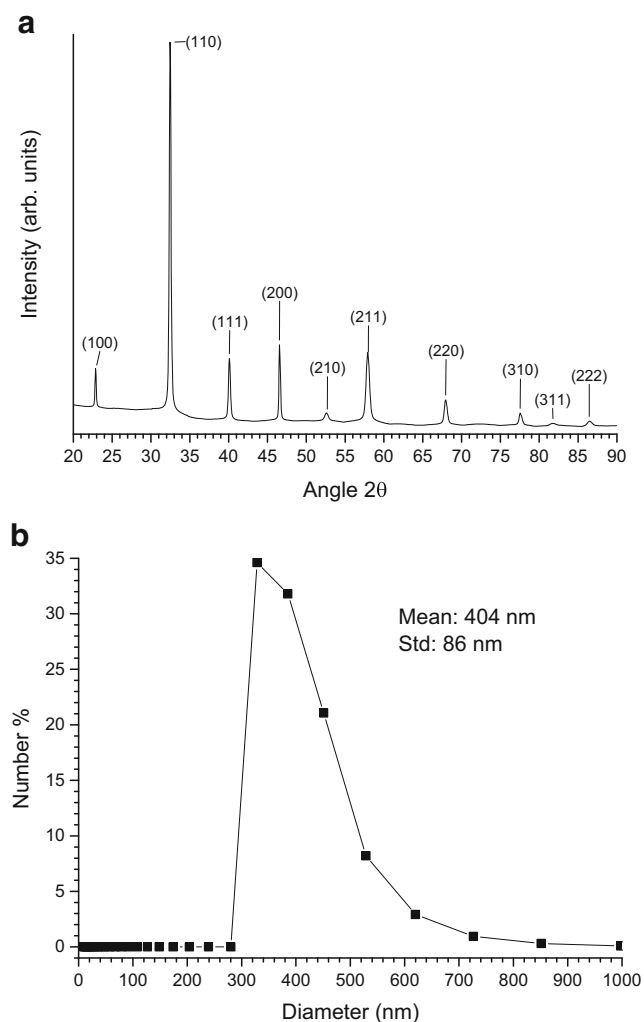


**Fig. 1** (a) XRD pattern and (b) particle size distribution of NBT-25ST powder calcined at 850°C for 3 h

phase. EDS analysis shows this phase to have a composition close to that of  $\text{SrTiO}_3$ , but with small amounts (<1 at. %) of Na and Bi. This could be an artefact caused by thermal etching. Single crystals of NBT-25ST grown at different temperatures for 10 h are shown in Fig. 3. Very little single crystal growth or matrix grain growth has taken place in the sample sintered at 1100°C. Increasing the sintering temperature to 1150°C causes a large increase in both single crystal growth and matrix grain growth. Further increases in sintering temperature cause a further increase in single crystal growth distance and matrix grain size.

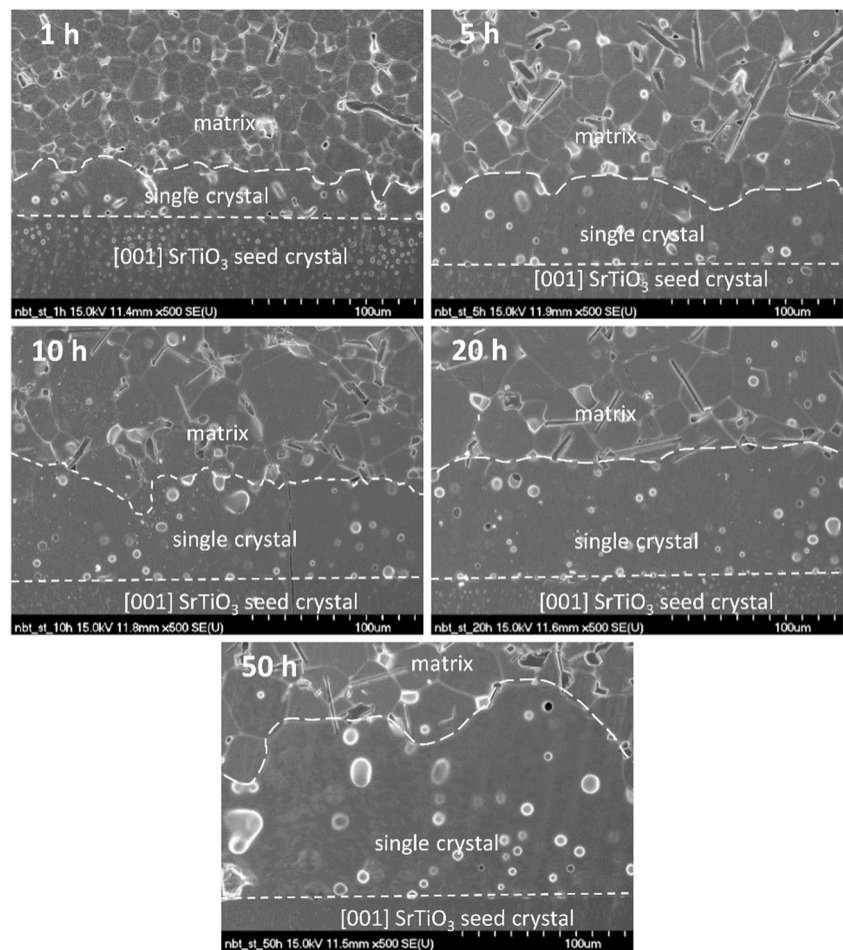
SEM micrographs of the matrix grains of samples sintered at different temperatures for 20 h are shown in Fig. 4. The grains in the samples sintered at 1100°C are much smaller than those sintered at higher temperatures (note the difference in magnification). The grains in the sample sintered at 1100°C are equiaxed and approximately equal in size, whereas abnormal grain growth has taken place in the samples sintered at

higher temperatures. Some of the grain boundaries in the samples show micro-faceting (marked with white arrows).

The results of the electron backscattered diffraction analysis of an NBT-25ST sample sintered at 1250°C for 5 h are shown in Fig. 5. Figure 5(a) shows an orientation map of the single crystal and seed. Figure 5(b) shows the corresponding grain boundary map. Figure 5(d) and (e) show an orientation and grain boundary map for the matrix region. The inverse pole figure for Fig. 5(a) and (d) is shown in the bottom of Fig. 5(f). From Fig. 5(a) and (b), it can be seen that a single crystal has grown epitaxially onto the seed crystal. The gradual change in colour across the seed and single crystal in Fig. 5(a) indicates a change in crystallographic orientation. This could be due to strains induced in the sample during polishing or strains due to a lattice mismatch between the seed crystal and single crystal. The multi-coloured blobs inside the single crystal are bad data points corresponding with the pores. The (001) pole figures of the single crystal region (top) and seed crystal region (bottom) in Fig. 5(c) show that the single crystal and seed regions have almost identical orientation. The slight change in orientation may be due to lattice mismatch between the seed crystal and single crystal. For each pole figure, an area  $\sim 40 \mu\text{m}$  in diameter was scanned. The orientation and grain boundary maps for the matrix region [Fig. 5(d) and (e)] clearly show their polycrystalline nature as does the (001) pole figure for the matrix region [Fig. 5(f)].

An optical micrograph of the NBT-25ST single crystal sample prepared for XRD is shown in Fig. 6(a). The single crystal and matrix regions can clearly be seen. Also, some matrix grains above the single crystal layer, which were not removed during polishing, can be seen. XRD patterns of this sample, a [001]  $\text{SrTiO}_3$  single crystal substrate and a NBT-25ST polycrystalline sample (which is in fact the NBT-25ST single crystal sample turned over to expose the polycrystalline matrix on the other side) are shown in Fig. 6(b). The NBT-25ST single crystal sample shows strong (100) and (200) peaks, which can be indexed with PDF#89–3109 for  $(\text{Na}_{0.5}\text{Bi}_{0.5})\text{TiO}_3$  (cubic, space group  $Pm-3m$ ). Very weak peaks corresponding to the surrounding matrix grains are also present, but they are too weak to be seen using a linear intensity scale. From the d-spacing of the (100) peak, the NBT-25ST single crystal has a unit cell parameter  $a = 3.89370 \text{ \AA}$ . The [001]  $\text{SrTiO}_3$  single crystal substrate can be indexed with PDF#84–0443 for  $\text{SrTiO}_3$  (cubic, space group  $Pm-3m$ ). From the d-spacing of the (100) peak, the [001]  $\text{SrTiO}_3$  single crystal substrate has a unit cell parameter  $a = 3.88957 \text{ \AA}$ . There is a small lattice mismatch between the seed crystal and single crystal which may cause the slight change in crystallographic orientation seen in the EBSD results. The NBT-25ST polycrystalline sample has an XRD pattern typical of a polycrystalline material which can be indexed with PDF#89–3109 for  $(\text{Na}_{0.5}\text{Bi}_{0.5})\text{TiO}_3$  (cubic, space group  $Pm-3m$ ). The small peaks to the right of the peaks, also visible in the (200) peaks

**Fig. 2** SEM micrographs of NBT-25ST samples sintered at 1200°C for 1–50 h. The white dashed lines mark the boundaries between the seed crystal/single crystal and the single crystal/matrix grains



for the NBT-25ST and SrTiO<sub>3</sub> single crystals, are caused by  $K\alpha_2$  splitting. The unit cell parameter as calculated by the least-squares method is  $3.89988 \pm 0.000157$  Å. The difference

in unit cell parameter between the NBT-25ST single crystal and polycrystalline samples may be due to a compressive stress placed on the single crystal by the seed crystal.

**Fig. 3** SEM micrographs of NBT-25ST samples sintered at 1100–1250°C for 10 h. The white dashed lines mark the boundaries between the seed crystal/single crystal and the single crystal/matrix grains

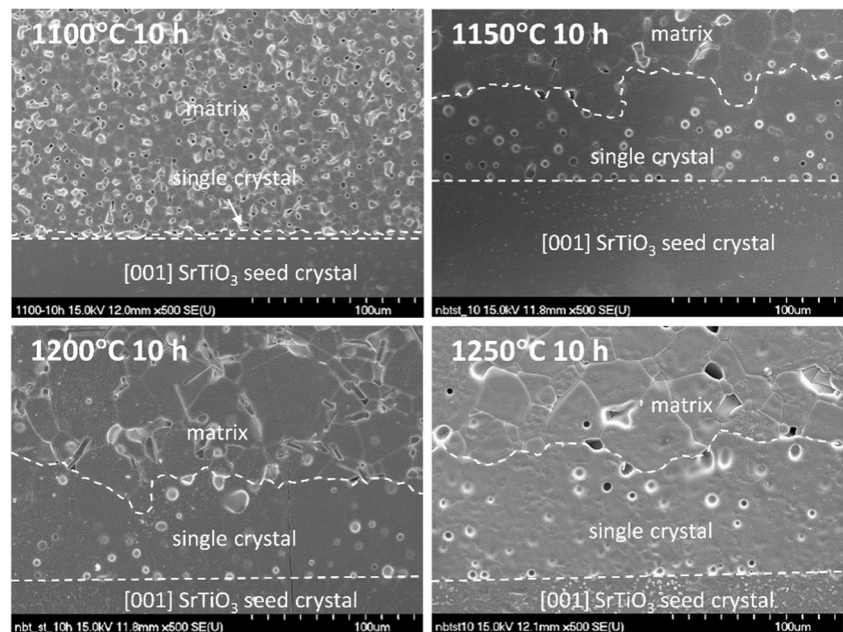
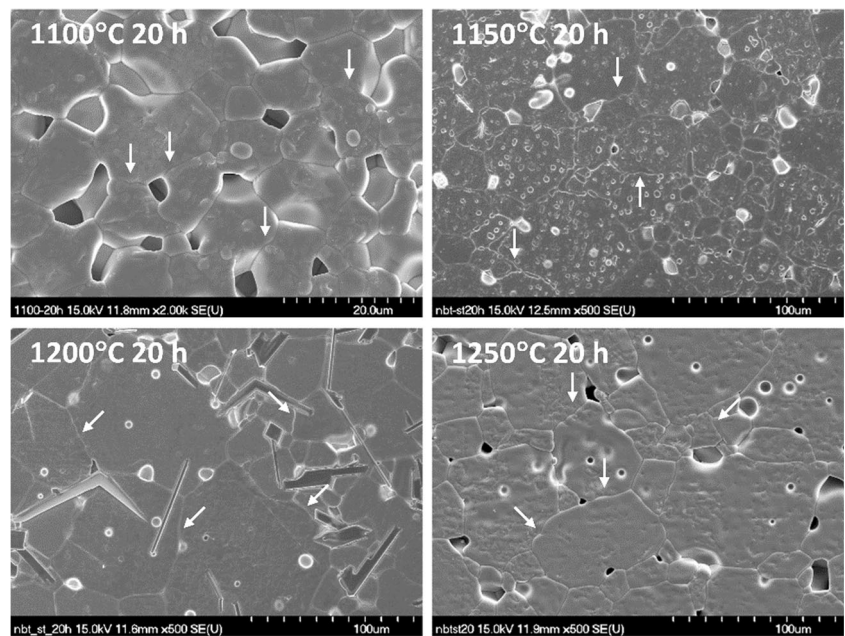


**Fig. 4** SEM micrographs of matrix grains of NBT-25ST samples sintered at 1100–1250°C for 20 h. White arrows mark micro-facets



The results of EDS analysis of the NBT-25ST samples sintered at 1100–1250°C for 10 h are given in Table 1, along with the nominal composition. The mean and standard

deviation of five points are given for each measurement. All of the samples are slightly Na-deficient, indicating that evaporation of Na<sub>2</sub>O has taken place during sintering.

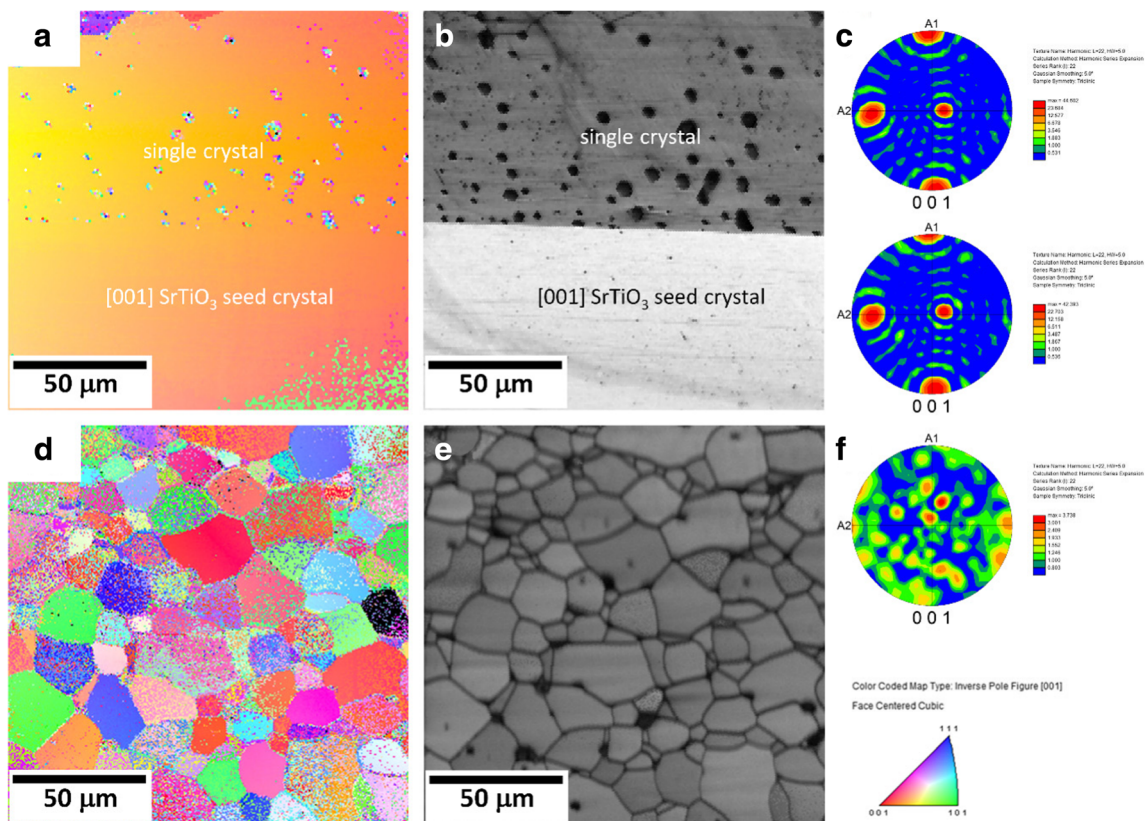


**Fig. 5** EBSD data of an NBT-25ST sample sintered at 1250°C for 5 h: (a) orientation map of single crystal and seed crystal region; (b) grain boundary map of the same region; (c) (001) pole figures of single crystal (top) and seed crystal (bottom) regions; (d) orientation map of

matrix region; (e) grain boundary map of same region; (f) (001) pole figure of matrix region. The inverse pole figure for parts (a) and (c) is shown in the bottom of part (f)

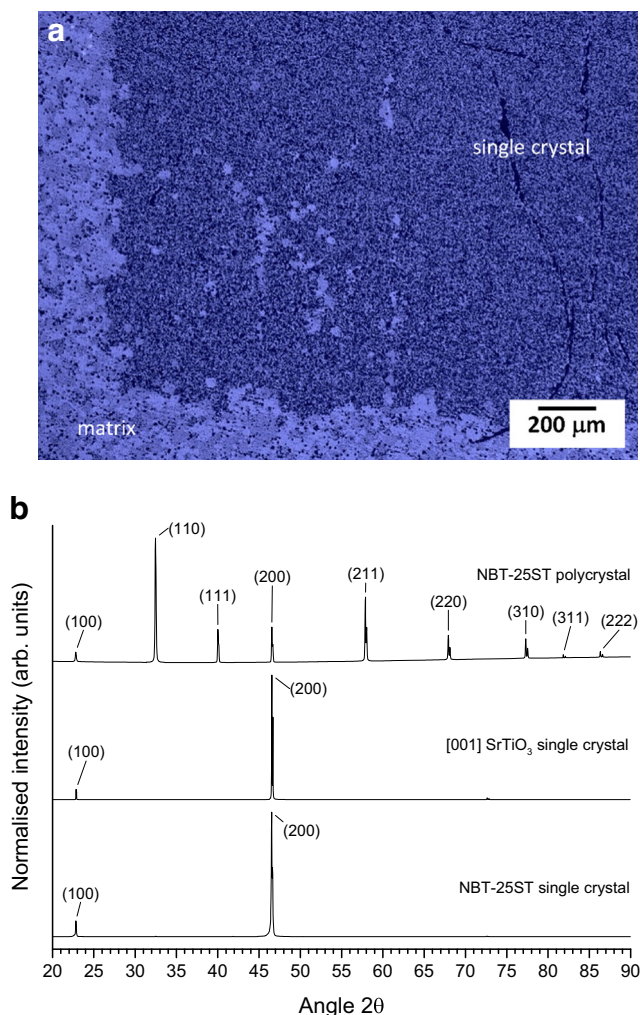


**Fig. 6** (a) Optical micrograph and (b) XRD patterns of NBT-25ST sample sintered at 1250°C for 5 h

Increasing the sintering temperature does not appear to have any effect on composition.

Figure 7 shows XPS spectra of a sample annealed at 1200°C for 10 h. The black lines are the original data, the blue peaks are mixed Gaussian-Lorentzian peaks fitted to the data, the red curves are the combinations of the fitted peaks and the green curves are the Shirley background. The O 1 s scan shows a main peak at a binding energy of 530.1 eV, with smaller peaks at 531.9, 533.5 and 528.4 eV. The peak at 530.1 eV is associated with oxygen anions bonded to metals [59, 60]. The peak at 531.9 eV may correspond to regions of the sample with O vacancies [59, 61]. The peak at 533.5 eV may be due to oxygen from OH<sup>-</sup> groups adsorbed on the sample surface or oxygen in surface sites [59, 61, 62]. The cause of the small peak at 528.4 eV is not known. The Na 1 s scan shows a main peak at 1071.7 eV, corresponding to the Na<sup>+</sup> ions [63] with smaller peaks at 1073.1, 1074.7, 1069.6, 1068.0 and 1066.8 eV. The cause of these extra peaks is not known, but could be due to non-stoichiometry at the sample

surface [62, 64]. The Ti 2p scan shows peaks at 458.7 eV and 464.7 eV that correspond to the Ti 2p<sub>3/2</sub> and Ti 2p<sub>1/2</sub> peaks of Ti<sup>4+</sup> [65, 66]. Extra peaks also appear at 457.2, 460.1, 463.1 and 466.4 eV. The presence of the low binding energy peaks at 457.2 and 463.1 eV indicate that some of the Ti<sup>4+</sup> cations have been reduced to Ti<sup>3+</sup> [60, 66]. The higher binding energy peaks may be due to non-stoichiometry at the sample surface [62, 64]. The Sr 3d scan shows peaks at 133.6 and 135.3 eV which correspond to the Sr 3d<sub>5/2</sub> and Sr 3d<sub>3/2</sub> peaks of the perovskite structure [62, 67]. The Bi 4f scan shows peaks at 157.0 and 162.3 eV, which correspond to the Bi 4f<sub>7/2</sub> and Bi 4f<sub>5/2</sub> peaks respectively in the trivalent oxidation state [65, 68]. Extra peaks also appear at 159.4 and 164.7 eV. The appearance of the extra peaks could be due to the formation of Bi vacancies [69, 70], non-stoichiometry at the sample surface [62, 64] or the existence of Bi cations in two coordination environments [71].

Backscattered electron images of the samples sintered at different temperatures for 10 h are shown in Fig. 8. Secondary phases can be seen between the matrix grains of the samples (marked with arrows). EDS analysis of these phases shows that the secondary phases in the samples sintered at 1100 and 1150°C consist primarily of Ti and O, with a composition close to TiO<sub>2</sub>. Secondary phases in the sample sintered at 1200°C contain Bi, Ti, Sr, Na and O but are deficient in Bi, Sr and Na compared to the matrix grains. The sample sintered at 1250°C shows the matrix grains, single crystal and seed crystal to the right of the micrograph. None of the samples show a core-shell microstructure in the matrix grains, as was previously observed by other workers [8, 55].

SEM micrographs of the powder samples annealed at different temperatures for 10 h and then air quenched are shown in Fig. 9. The powder annealed at 1100°C consists of grains with flat faces (marked with arrows) and smoothly curved edges and corners. An increase in annealing temperature to 1150°C causes the flat faces to grow larger. In the samples annealed at 1200 and 1250°C, growth steps can be seen at the edges and corners of the grains. TEM micrographs of the ceramic samples sintered at 1100 and 1150°C for 1 h are shown in Fig. 10, along with selected area diffraction patterns from the matrix grains. In both samples the grains are equiaxed and pockets of a secondary phase are visible at the triple junctions. Some of the grain boundaries appear faceted whereas others appear curved. The interfaces between the grains and the secondary phase at the triple junctions are curved in the sample sintered at 1100°C [Fig. 10(b)] but are more faceted in the sample sintered at 1150°C [Fig. 10(d)]. EDS analysis showed that the secondary phase in the sample sintered at 1150°C contains more Bi and less Na than the secondary phase of the sample sintered at 1100°C (Table 2). The core-shell microstructure observed by Acosta et al. was not present in the samples [8]. A sample for TEM analysis was also sintered at

**Table 1** EDS analysis of NBT-25ST samples sintered at 1100–1250°C for 10 h

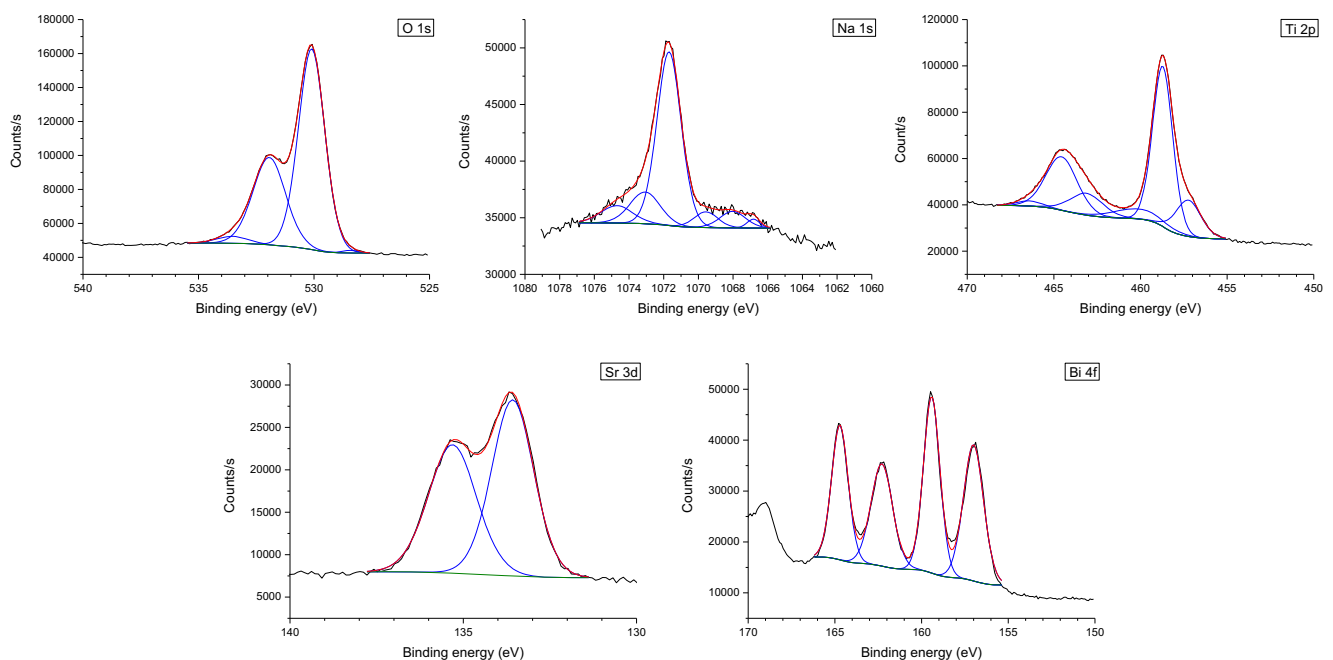
	1100°C		1150°C		1200°C		1250°C		Nominal
	Single crystal	Matrix	Single crystal	Matrix	Single crystal	Matrix	Single crystal	Matrix	
O	61.04 ± 0.80	61.21 ± 2.41	60.01 ± 1.11	58.56 ± 1.77	61.00 ± 1.58	60.16 ± 0.58	60.73 ± 0.84	61.09 ± 2.04	60
Na	6.22 ± 0.25	6.11 ± 0.48	6.13 ± 0.64	6.57 ± 0.76	6.55 ± 0.48	6.46 ± 0.34	6.22 ± 0.60	6.03 ± 0.53	7.5
Ti	19.30 ± 0.81	19.73 ± 1.26	20.08 ± 1.06	20.57 ± 0.95	19.24 ± 0.78	19.72 ± 0.37	19.55 ± 0.76	19.73 ± 0.95	20
Sr	5.49 ± 0.18	5.18 ± 1.00	5.76 ± 0.47	5.97 ± 0.23	5.51 ± 0.40	5.67 ± 0.13	5.52 ± 0.27	5.39 ± 0.29	5
Bi	7.95 ± 0.22	7.78 ± 0.62	8.03 ± 0.17	8.32 ± 0.54	7.69 ± 0.35	7.98 ± 0.18	7.99 ± 0.31	7.76 ± 0.65	7.5

1250°C for 1 h, but due to the large grain size, the sample prepared by FIB did not have any grain boundaries.

Single crystal growth distance as a function of sintering time and temperature is shown in Fig. 11. The single crystal growth distance depends on sintering time as well as temperature. The growth distance at 1100°C is low and increases slowly with sintering time. An increase in sintering temperature to 1150°C or 1200°C results in a considerable increase in growth distance. In the samples sintered at 1150 and 1200°C, the initial growth rate is rapid but then tails off with sintering time. At a sintering temperature of 1250°C, single crystal growth is rapid for the first 5 h of sintering, but then becomes slow. Despite rapid initial growth, the single crystal growth distance for the sample sintered at 1250°C for 50 h is slightly smaller than that of the sample sintered at 1200°C. The maximum single crystal growth distance of the NBT-25ST samples is  $\sim 107 \pm 18 \mu\text{m}$  after sintering at 1200°C for 50 h. The error bars indicate that the single crystal growth distance varies across each sample, as can also be seen in Figs. 2 and 3.

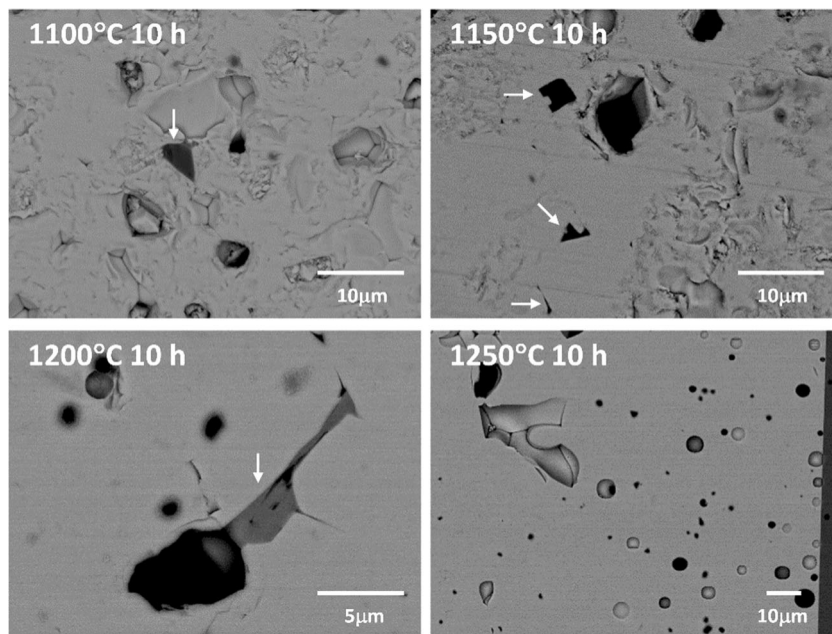
The mean matrix grain size (2D equivalent radius) of the samples is shown in Fig. 12. The grains of the secondary phases were ignored when measuring grain sizes. The mean grain size also depends strongly on sintering time and temperature. For the samples sintered at 1100°C, matrix grain growth is slow but steadily continues for 20 h and then the grain growth rate starts to slow. For the samples sintered at higher temperatures, grain growth rate levels off after 10 h. The maximum matrix grain size is  $13 \pm 10 \mu\text{m}$  after sintering at 1250°C for 50 h. The matrix grain growth behavior looks similar to the single crystal growth behavior. The large error bars indicate that the grain size distributions in the samples are very broad. This is particularly seen in the samples sintered at 1250°C.

Figure 13 shows the grain size distributions of all the samples sintered at 1100, 1150, 1200 and 1250°C respectively. The grain size distributions of all samples sintered at 1100°C slowly broaden with increased sintering time, but remain relatively narrow and unimodal, even after sintering for 50 h. Such grain size

**Fig. 7** XPS spectra of an NBT-25ST sample sintered at 1200°C for 10 h



**Fig. 8** SEM backscattered electron images of NBT-25ST samples sintered at 1100–1250°C for 10 h. White arrows mark secondary phases

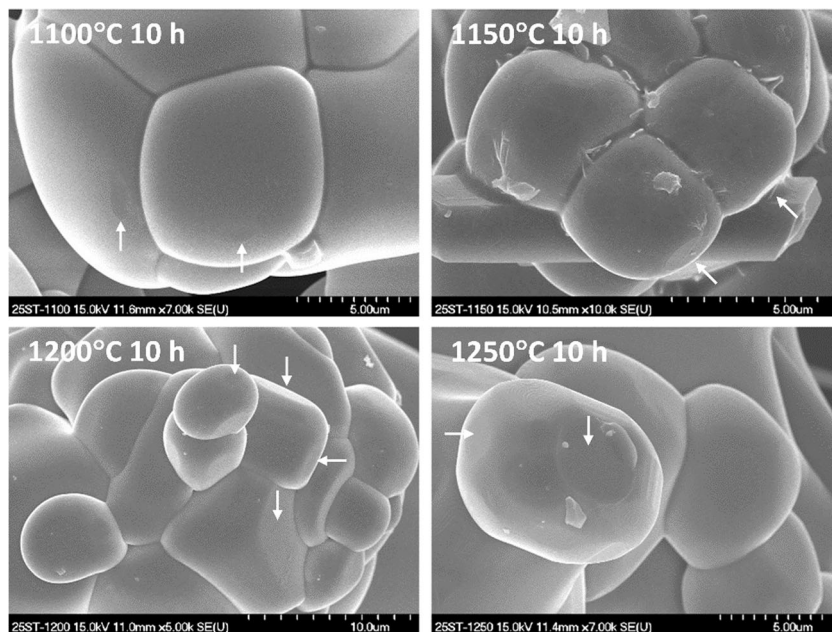


distributions are characteristic of normal grain growth. At 1150, 1200 and 1250°C the grain size distributions rapidly become broad, which is characteristic of abnormal grain growth. The grain size distributions broaden more rapidly as sintering temperature increases. For the samples sintered at 1150°C, the grain size distribution has broadened after 5 h of sintering. For the samples sintered at 1200 and 1250°C, broadening of the grain size distribution has already taken place after 1 h. The grain size distributions become broader as sintering time increases. The grain size distributions indicate that the grains start growing abnormally after 5 h for the samples sintered at 1150°C and after 1 h for the samples sintered at 1200 and 1250°C.

#### 4 Discussion

The SEM micrographs show that single crystals of NBT-25ST can be successfully grown on [001] SrTiO<sub>3</sub> seed crystals (Figs. 2 and 3). The EBSD and XRD results show that the NBT-25ST single crystals grow epitaxially on the [001] SrTiO<sub>3</sub> seed crystals (Figs. 5 and 6). EDS and XPS analysis show that volatilization of Na and formation of O vacancies take place during sintering (Table 1 and Fig. 7). Although Bi loss was not detected by EDS, the presence of the extra peaks in the Bi 4f XPS spectrum indicates the possible formation of Bi vacancies (Fig. 7). Loss of volatile elements such as Na and

**Fig. 9** SEM micrographs of NBT-25ST powder annealed at 1100–1250°C for 10 h and quenched in air. White arrows mark flat faces



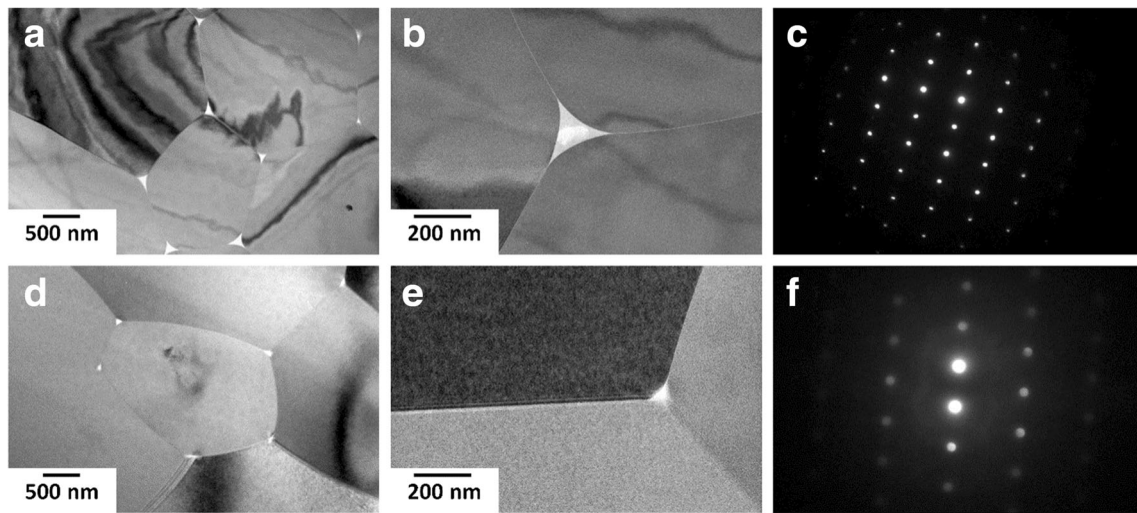
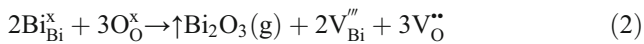
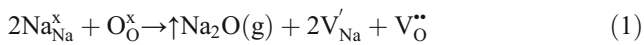


**Fig. 10** TEM micrographs of matrix grains of NBT-25ST samples sintered at (a), (b) 1100°C and (d), (e) 1150°C for 1 h. SADPs of the matrix grains of samples sintered at 1100 and 1150°C are shown in (c) and (f) respectively

Bi during prolonged sintering is expected based on previous work [51]. Loss of volatile elements could take place via the following defect reactions:



Oxygen vacancies can also form according to the reaction:



The free electrons may then reduce  $\text{Ti}^{4+}$  to  $\text{Ti}^{3+}$ , accounting for the low binding energy peaks in the Ti 2p XPS spectrum (Fig. 7). The use of Na- and Bi-excess NBT packing powders was found to be effective in reducing loss of Na and Bi [54].

The single crystal and matrix grain growth behavior of NBT-25ST can be interpreted using the mixed control mechanism of microstructural evolution [47, 56, 57, 72]. The single crystal and grain growth behavior depends on the atomic structure of the interfaces, which can be ordered (smooth/faceted) or disordered (rough) [73–76]. For a system with solid/liquid interfaces, the driving force for grain growth  $\Delta G$  is given by [73, 76–78]:

$$\Delta G = 2\gamma\Omega \left( \frac{1}{\bar{r}} - \frac{1}{r} \right) \quad (4)$$

Where  $\gamma$  is the solid/liquid interfacial energy,  $r$  the radius of the grain of interest,  $\Omega$  the molar volume and  $\bar{r}$  the radius for a critical grain that neither grows nor shrinks (usually the mean grain radius or a value close to it).

For a system with disordered interfaces, there are an unlimited number of sites at which atoms can attach to or detach from the surface of the grain. In this case, grain growth is limited by the rate at which atoms diffuse through the liquid phase to the growing grain. The growth rate increases linearly with driving force (the dashed line in Fig. 14) and all grains with  $\Delta G > 0$  can grow. In this case, single crystal and abnormal grain growth will not occur and the relative size distribution of the grains ( $r/\bar{r}$ ) is invariant with annealing time [73, 74]. The grain growth rate for diffusion-controlled growth is given by [79]:

$$\frac{dR}{dt} = \frac{2\beta}{\delta} \left( \frac{1}{\bar{r}} - \frac{1}{r} \right) \quad (5)$$

$\beta = (DS\Omega\gamma/kT\rho)$  where  $D$  is the diffusion coefficient of the solid phase in the liquid,  $S$  is the true solubility of the solid phase in the liquid,  $k$  the Boltzmann constant,  $T$  the absolute temperature and  $\rho$  the density of the solid phase.  $\delta$  is the thickness of the intergranular liquid phase. In this equation,  $\bar{r}$  equals 9/8 times the mean grain radius.

**Table 2** EDS analysis of secondary phases of NBT-25ST samples sintered at 1100 and 1150°C for 1 h

	Na (at. %)	Ti (at. %)	Sr (at. %)	Bi (at. %)
1100°C, second phase, point 1	44.7	30.0	23.4	1.7
1100°C, second phase, point 2	46.6	47.9	4.6	1.0
1150°C, second phase, point 1	38.3	43.6	8.0	10.2
1150°C, second phase, point 2	28.0	46.3	10.2	15.6

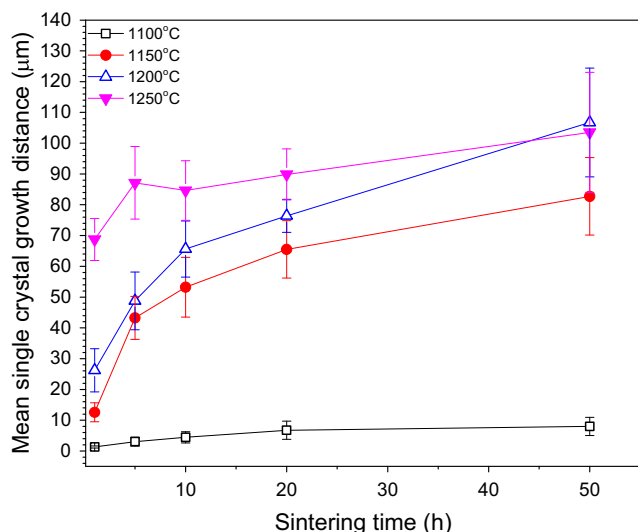


Fig. 11 Single crystal growth distance as a function of sintering time and temperature

For a system with ordered interfaces, atoms cannot easily attach to the surface of the grain due to their large number of broken bonds. Two-dimensional nuclei or screw dislocations, which can provide low energy sites for atom attachment, need to be present for the growth of grains. This causes the relationship between the grain growth rate and the driving force for growth to take on a nonlinear form [47, 56, 57, 72, 76, 77]. For a system in which the nucleation and growth of 2D nuclei controls grain growth, the rate of formation of stable 2D nuclei depends exponentially on  $\Delta G$  [80, 81]. Below a critical driving force  $\Delta G_c$ , few stable nuclei form and grain growth is very slow. The grain growth rate for  $\Delta G \leq \Delta G_c$  is given by [72, 82]:

$$\frac{dR}{dt} = B \exp\left(-\frac{C}{\frac{1}{\bar{r}} - \frac{1}{r}}\right) \tag{6}$$

$B = (hA\psi n_0)$  where  $h$  is the step height of the 2D nucleus,  $A$  is the grain facet size and  $n_0$  is the number density of atoms in the liquid.  $\psi = n^* \nu \exp(\Delta g_m/kT)$ , where  $n^*$  is the number of atoms in a position near to a critical 2D nucleus,  $\nu$  is the vibration frequency of atoms in the liquid and  $\Delta g_m$  is the activation energy for jumping across the liquid/solid interface.  $C = (\pi \epsilon^2/6kT\gamma)$ , where  $\epsilon$  is the step free energy (the excess energy due to the presence of the step). For  $\Delta G > \Delta G_c$ , kinetic roughening of the grain surfaces takes place [83–85]. The rate of formation of 2D nuclei becomes so high that atoms can easily attach at any site on the grain surface and the grain growth rate becomes diffusion-limited, as in Eq. (2). The grain growth rate increases exponentially at  $\Delta G \approx \Delta G_c$  and then increases linearly with further increase in  $\Delta G$  (the solid line in Fig. 14). Grains with  $\Delta G < 0$  will shrink following a linear dependence with  $\Delta G$ , as atoms can detach from each corner of the grain without an energy barrier [72].

The value of  $\Delta G_c$  is given by [56, 72, 82]:

$$\Delta G_c = \frac{\pi \epsilon^2}{kTh} (\ln \psi n_0)^{-1} \tag{7}$$

It can be seen that  $\Delta G_c$  varies with the square of the step free energy  $\epsilon$ .  $\epsilon$  in turn varies with sintering atmosphere, dopant addition and sintering temperature [49, 86, 87].  $\epsilon$  decreases exponentially with increasing temperature according to [72, 88]:

$$\epsilon \propto \exp\left(-\frac{M}{\sqrt{T_r - T}}\right) \tag{8}$$

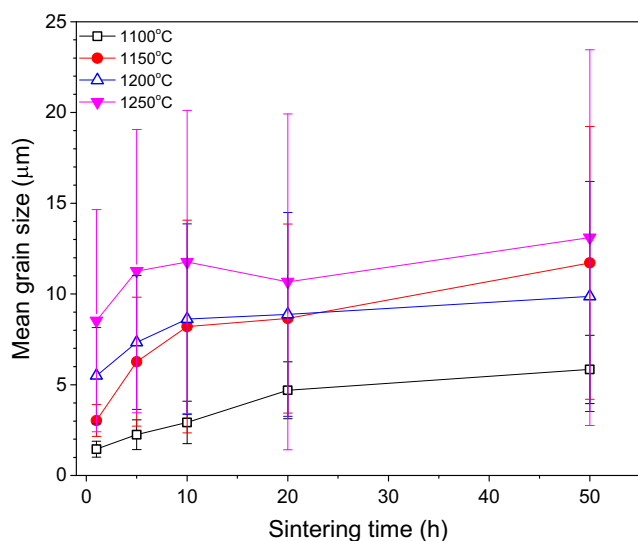
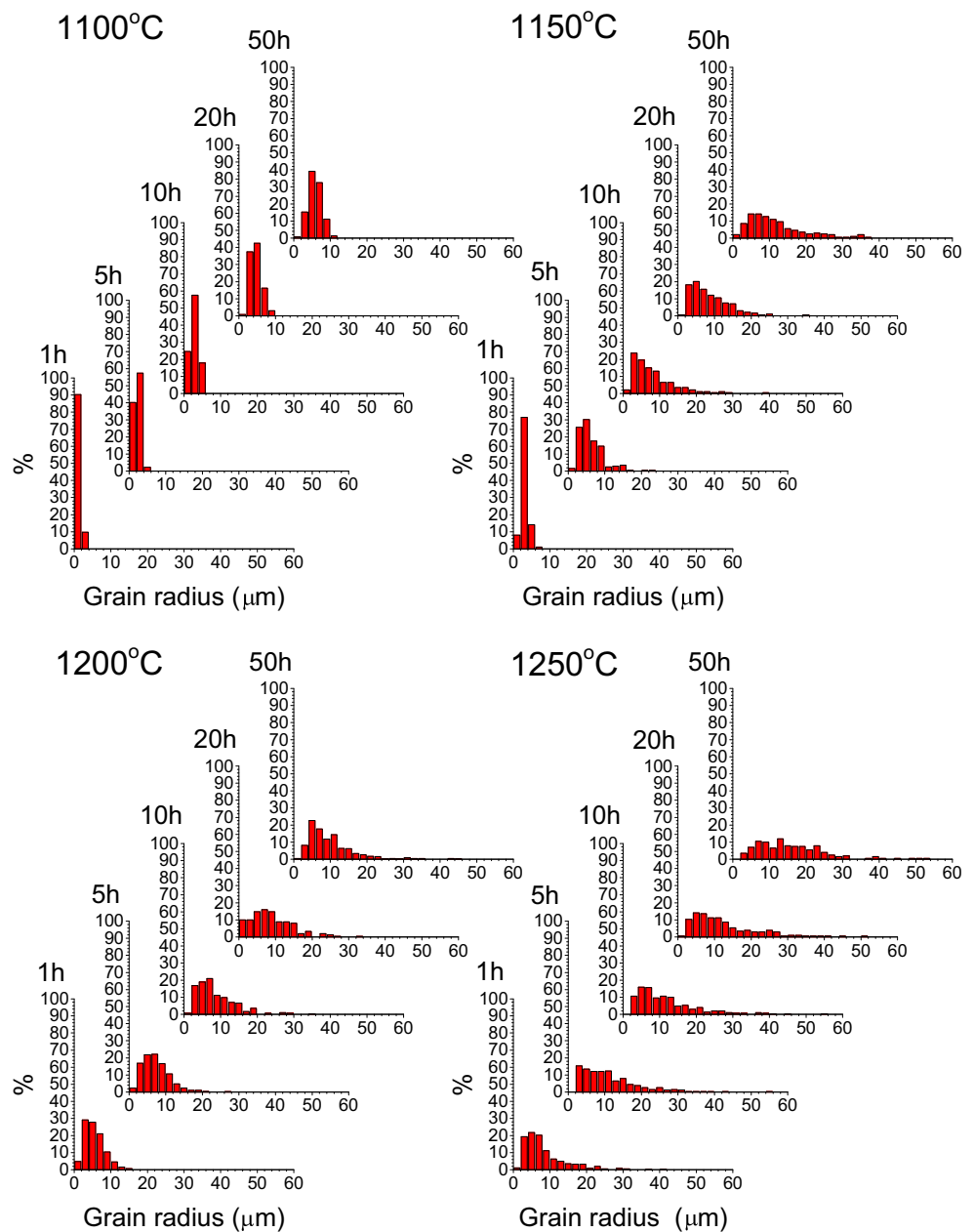


Fig. 12 Mean matrix grain size as a function of sintering time and temperature

$M$  is a constant and  $T_r$  is the roughening temperature, where the surface structure of the grain changes from ordered to disordered. By varying the sintering temperature, the value of  $\Delta G_c$  can be changed and this in turn affects the grain growth behavior [56, 72, 82]. Varying the sintering temperature will also affect the diffusion coefficient  $D$  and the true solubility  $S$ , which will affect the growth rate of the grains with values of  $\Delta G \geq \Delta G_c$ .

For a system controlled by 2D nucleation and growth, the type of grain growth behavior that takes place depends on the relative values of  $\Delta G_c$  and  $\Delta G_{max}$  ( $\Delta G_{max}$  is the maximum driving force for the largest grain in the system). If  $\Delta G_c = 0$ , the growth of all grains is linearly proportional to their driving force and the grain growth behavior is normal. If  $\Delta G_c < \Delta G_{max}$ , the grain growth is pseudo-normal. A large number of grains have  $\Delta G > \Delta G_c$  and can grow. As a result, the growth behavior is similar to normal grain growth behavior. If  $\Delta G_c \leq \Delta G_{max}$ , the grain growth is abnormal. Most of the

**Fig. 13** Grain size distributions as a function of sintering time and temperature



matrix grains have  $\Delta G < \Delta G_c$  and grow very slowly. A small number of grains have  $\Delta G \geq \Delta G_c$ . These grains grow rapidly and consume the grains surrounding them to become much larger compared to other grains. Such grains are called abnormal grains. If  $\Delta G_c \gg \Delta G_{\max}$ , none of the grains have a driving force large enough for appreciable growth and grain growth is essentially stagnant [56, 73, 77]. In the SSCG method, the seed single crystal is much larger than the surrounding matrix grains. It has a driving force  $> \Delta G_c$  and acts like an abnormal grain. A single crystal grows on the seed crystal and consumes the surrounding matrix grains [44, 46, 89]. Grains in the matrix can also grow abnormally if they are large

enough to have  $\Delta G \geq \Delta G_c$ . Similar behavior has also been found to occur in solid state sintered systems [56, 90, 91].

The grain shape in the  $(\text{Na}_{0.5}\text{Bi}_{0.5})\text{TiO}_3\text{-BaTiO}_3$  system is faceted with rounded edges and corners [92]. In such a system, the grain growth is governed by the growth of the faceted interfaces [92, 93]. The grain shape in the present NBT-25ST system is also faceted with rounded edges and corners (Figs. 4, 9 and 10). The grain growth is therefore controlled by the 2D nucleation and growth or screw dislocation growth methods, as outlined above. The rounded corners and edges of the grains implies that the step free energy  $\epsilon$  in this system is low [78, 92, 94–96]. In the samples sintered at 1100°C, the

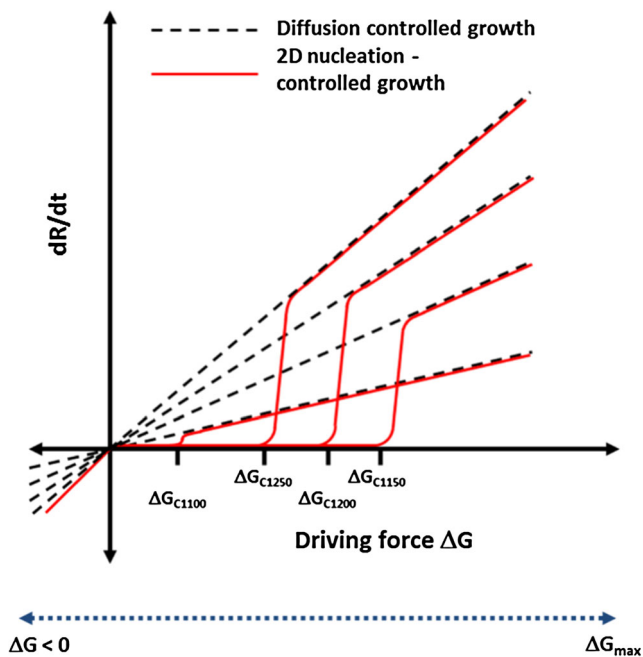


**Fig. 14** Schematic plot of grain growth rate vs. driving force for growth for systems in which diffusion-controlled growth and 2D nucleation-controlled growth take place

value of  $\Delta G_c$  is low due to the low value of step free energy  $\epsilon$  (Eq. 7) and so pseudo-normal grain growth takes place. Both the seed crystal and many of the matrix grains have values of  $\Delta G > \Delta G_c$  and so can grow. The grain size distribution remains unimodal even after long sintering times (Fig. 13). Due to the low sintering temperature, the growth rate of both the single crystal and matrix grains is very slow (Figs. 11 and 12). It is notable that the single crystal growth distance and mean matrix grain sizes are very similar in the samples sintered at 1100°C. Because many matrix grains are also growing, the seed crystal does not have a growth advantage over the matrix grains and so cannot grow abnormally.

As the sintering temperature increases to 1150°C, the increase in the area of the flat faces on the grains (Fig. 9) indicates an increase in the step free energy  $\epsilon$  [78, 94, 96, 97]. The change in the shape of the solid/liquid interfaces at the triple junctions from curved to faceted also indicates an increase in  $\epsilon$  (Fig. 10) [74]. Consequently  $\Delta G_c$  also increases (Eq. 7). This reduces the number of matrix grains with  $\Delta G > \Delta G_c$  that are able to grow; however, there are still numerous matrix grains with  $\Delta G > \Delta G_c$  that can grow. The seed crystal also has  $\Delta G > \Delta G_c$  and so a single crystal can grow. The growth rate of the single crystal and the growing matrix grains will increase because of an increase in the diffusion coefficient  $D$  and increased solubility of the solid phase in the liquid  $S$  (Eq. 5). From Figs. 12 and 13 it can be seen that the mean matrix grain size increases but that the grain size distribution initially remains unimodal. As the matrix grains grow, the mean grain size  $\bar{r}$  increases, causing a decrease in the values of  $\Delta G$  for the

growing grains (Eq. 4). As the value of  $\Delta G$  for a particular grain drops below  $\Delta G_c$ , it stops growing. Eventually, most of the matrix grains stop growing. Because the seed crystal is much larger than the matrix grains, it still has  $\Delta G > \Delta G_c$  and can continue to grow (Figs. 3 and 11). Some matrix grains will also still have  $\Delta G > \Delta G_c$  and can continue growing to form abnormal grains, causing the grain size distribution to broaden (Fig. 13). The grain growth behavior changes from pseudo-normal to abnormal. This takes place by 5 h of sintering. Similar behavior was previously observed in  $(\text{Na}_{0.5}\text{Bi}_{0.5})\text{TiO}_3\text{-BaTiO}_3$  [92, 98].

Further increase in sintering temperature to 1200°C cause  $\epsilon$  and  $\Delta G_c$  to decrease (Eqs. 7 and 8). This increases the number of grains with  $\Delta G > \Delta G_c$  that are able to grow and therefore should delay the point at which the grain growth behavior changes from pseudo-normal to abnormal. However, this is compensated for by the further increase in the growth rate of matrix grains due to increases in  $D$  and  $S$ . The rapid matrix grain growth causes the growth behavior to shift from pseudo-normal to abnormal by 1 h of sintering. The growth rate of the abnormal grains also increases, causing the grain size distribution to rapidly broaden. Increasing the sintering temperature to 1250°C accelerates this process. Increasing the sintering temperature also causes increased single crystal growth due to increased values of  $D$  and  $S$ .

The matrix grain size is important because of its direct correlation to the driving force for single crystal growth (Eq. 4). As the mean matrix grain size increases, the driving force for single crystal growth decreases, causing single crystal growth to tail off as sintering time increases (Fig. 11). The large values of mean grain size in the samples sintered at 1250°C reduce the driving force for single crystal growth and so the growth distance of the samples sintered at 1200 and 1250°C converge after sintering for 50 h. In addition to the large mean grain size, abnormal grains in the matrix will impinge on the single crystal layer and prevent single crystal growth. This impingement effect may be the cause for variations in the single crystal growth rate in a particular sample, as shown by the error bars in Fig. 11. From the results, the optimum temperature for single crystal growth is 1250°C as a growth distance of  $\sim 90 \mu\text{m}$  can be obtained after just 5 h.

Single crystals grown by the SSCG method usually contain many pores. These pores in the single crystal come from the matrix due to the fast movement of the interface between the growing single crystal and the matrix, which causes pores at the single crystal/matrix grain boundary to be trapped within the single crystal [44, 48]. Moreover, due to coalescence the pores in the matrix can increase in size [44, 99]. The shape of the pores trapped inside the single crystal and matrix grains gives an indication of the equilibrium grain shape [100]. For  $(\text{K}_{0.5}\text{Na}_{0.5})\text{NbO}_3$ -based systems, intergranular pores are usually cubic in shape, indicating that these systems have a high value of step free energy  $\epsilon$  [49, 100]. However, in the present

work, the pores trapped in the single crystal and matrix grains are spherical, indicating that the  $(\text{Na}_{0.5}\text{Bi}_{0.5})\text{TiO}_3$ - $\text{SrTiO}_3$  system has a low step free energy [78]. Similar results have been found in other  $(\text{Na}_{0.5}\text{Bi}_{0.5})\text{TiO}_3$ -based systems [52]. Porosity in the single crystal can be reduced by combining hot pressing with crystal growth [101] or two-step sintering [102] to increase the sample density.

The behavior of the NBT-25ST samples with temperature is somewhat unusual. From Eq. (8), the step free energy  $\epsilon$  is expected to decrease continuously as sintering temperature increases. An increase in vacancy concentration with increased sintering temperature is also expected to reduce  $\epsilon$  [103]. However, from the shape of the annealed powders (Fig. 9) and of the solid/liquid interfaces at the triple junctions (Fig. 10), the step free energy appears to increase as the sintering temperature increases from 1100 to 1150°C. Further increases in temperature cause  $\epsilon$  to decrease as expected. The reason for this increase in  $\epsilon$  between 1100 and 1150°C is not clear. Koruza et al. studied NBT-25ST ceramic samples sintered at 1150°C for 2–20 h and found them to possess a core-shell microstructure with a BNT-rich core and a ST-rich shell [55]. Extended sintering caused the core-shell microstructure to disappear due to interdiffusion between the core and the shell. In the present work, it could be possible that increasing the sintering temperature from 1100 to 1150°C caused the core-shell microstructure in the matrix grains to disappear. This would change the chemical composition of the grain surface and hence the step free energy. However, no evidence of a core-shell microstructure was found in the matrix grains of samples sintered at any temperature (Fig. 8). After 10 h of sintering, the core-shell microstructure could have already disappeared from our samples, but Koruza et al. found that the core-shell microstructure persisted even in samples sintered at 1150° for 20 h. Also, a core-shell microstructure was not present in the samples sintered at 1100 and 1150°C for 1 h (Fig. 10). Therefore it is unlikely that changes in the core-shell microstructure are responsible for the behavior of our NBT-25ST samples. The increase in  $\epsilon$  with sintering temperature between 1100 and 1150°C could be caused by changes in the chemical composition of the liquid phase at the triple junctions (Table 2). Previous work in the 95 mol%  $(\text{Na}_{0.5}\text{Bi}_{0.5})\text{TiO}_3$ -5 mol%  $\text{BaTiO}_3$  system has shown that addition of  $\text{TiO}_2$  caused changes in the grain growth behavior consistent with an increase in step free energy  $\epsilon$  [98]. Changes in stoichiometry can also affect the grain growth behavior [104, 105]. The grain growth behavior of this system needs to be studied in greater detail.

## 5 Conclusions

Single crystals of NBT-25ST were grown by SSCG on [001] oriented  $\text{SrTiO}_3$  seed crystals for the first time. Electron

backscattered diffraction and X-ray diffraction analysis shows that the single crystals have grown epitaxially on the seed crystals. Energy dispersive spectroscopy analysis shows the single crystals to be slightly Na-deficient. X-ray photoelectron spectroscopy indicates the presence of oxygen vacancies. The dependence of single crystal growth and matrix grain growth on sintering temperature and time was studied. Samples sintered at 1100°C showed little single crystal and matrix grain growth. Increasing the sintering temperature to  $\geq 1150^\circ\text{C}$  caused an increase in single crystal growth distance and mean matrix grain size, as well as abnormal grain growth in the matrix. At long sintering times, the single crystal growth distance for samples sintered at 1200 and 1250°C converges. The optimum single crystal growth temperature is found to be 1250°C. The single crystal and grain growth behavior can be explained using the mixed control mechanism of microstructural evolution.

**Acknowledgements** This research was supported by the Basic Science Research Program through the National Research Foundation of Korea (NRF), funded by the Ministry of Education (grant no. 2015R1D1A1A01057060). The authors would like to thank Kyeong-Kap Jeong, Ji-Hyeon Lee, Hey-Jeong Kim and Ji-Won Na for operating the XRD, particle size analyser, SEM and XPS respectively, and Kyung-Soon Kim (National Nanofab Center, Daejeon) for operating the EBSD. The authors would also like to thank Zhao Zhiqiang for assistance with the powder annealing and air quenching experiments.

## References

1. J. Rödel, W. Jo, K.T.P. Seifert, E.-M. Anton, T. Granzow, D. Damjanovic, *J. Am. Ceram. Soc.* **92**(6), 1153 (2009)
2. A.J. Moulson, J.M. Herbert, *Electroceramics: Materials, Properties, Applications*. 2nd Edn, (John Wiley & Sons, Chichester, 2005), pp. 339-410.
3. M. Villafuerte-Castrejón, E. Morán, A. Reyes-Montero, R. Vivar-Ocampo, J.-A. Peña-Jiménez, S.-O. Rea-López, L. Pardo, *Materials* **9**(1), 21 (2016)
4. W. Jo, R. Dittmer, M. Acosta, J. Zang, C. Groh, E. Sapper, K. Wang, J. Rödel, *J. Electroceram.* **29**(1), 71 (2012)
5. Q. Li, S. Gao, L. Ning, H. Fan, Z. Liu, Z. Li, *Ceram. Int.* **43**(7), 5367 (2017)
6. W. Bai, D. Chen, P. Zheng, J. Zhang, F. Wen, B. Shen, J. Zhai, Z. Ji, *J. Alloys Compd.* **709**, 646 (2017)
7. S.-Y. Choi, S.-J. Jeong, D.-S. Lee, M.-S. Kim, J.-S. Lee, J.H. Cho, B.I. Kim, Y. Ikuhara, *Chem. Mater.* **24**(17), 3363 (2012)
8. M. Acosta, L.A. Schmitt, L. Molina-Luna, M.C. Scherrer, M. Brilz, K.G. Webber, M. Deluca, H.-J. Kleebe, J. Rödel, W. Donner, *J. Am. Ceram. Soc.* **98**(11), 3405 (2015)
9. C.W. Ahn, G. Choi, I.W. Kim, J.-S. Lee, K. Wang, Y. Hwang, W. Jo, *NPG Asia Mater* **9**, e346 (2017)
10. W. Bai, D. Chen, P. Zheng, J. Xi, Y. Zhou, B. Shen, J. Zhai, Z. Ji, *J. Eur. Ceram. Soc.* **37**(7), 2591 (2017)
11. R.Z. Zuo, H. Qi, J. Fu, J.F. Li, M. Shi, Y.D. Xu, *Appl. Phys. Lett.* **108**(23), 5 (2016)
12. C. Chen, X. Zhao, Y. Wang, H. Zhang, H. Deng, X. Li, X. Jiang, X. Jiang, H. Luo, *Appl. Phys. Lett.* **108**(2), 022903 (2016)
13. T. Zheng, J. Wu, X. Cheng, X. Wang, B. Zhang, D. Xiao, J. Zhu, X. Wang, X. Lou, *J. Mater. Chem. C* **2**(41), 8796 (2014)

14. K. Praveena, K.B.R. Varma, *J. Mater. Sci.: Mater. Electron* **25**(1), 111 (2014)
15. K. Praveena, K.B.R. Varma, *J. Mater. Sci.: Mater. Electron* **25**(12), 5403 (2014)
16. J. Koruza, B. Rožič, G. Cordoyiannis, B. Malič, Z. Kutnjak, *Appl. Phys. Lett.* **106**(20), 202905 (2015)
17. J. Li, Y. Bai, S. Qin, J. Fu, R. Zuo, L. Qiao, *Appl. Phys. Lett.* **109**(16), 162902 (2016)
18. C. Cui, Y. Pu, Z. Gao, J. Wan, Y. Guo, C. Hui, Y. Wang, Y. Cui, *J. Alloys Compd.* **711**, 319 (2017)
19. T. Shao, H. Du, H. Ma, S. Qu, J. Wang, J. Wang, X. Wei, Z. Xu, *J. Mater. Chem. A* **5**(2), 554 (2017)
20. G. Smolenskii, V. Isupov, A. Agranovskaya, N. Krainik, *Sov. Phys. Solid State* **2**(11), 2651 (1961)
21. G.O. Jones, P.A. Thomas, *Acta Crystallogr. B* **58**(2), 168 (2002)
22. Y.-Q. Lu, Y.-X. Li, *J. Adv. Dielectr.* **01**(03), 269 (2011)
23. K. Roleder, J. Suchanicz, A. Kania, *Ferroelectrics* **89**, 1–5 (1989)
24. J. Suchanicz, K. Roleder, A. Kania, *J. Hańaderek, Ferroelectrics* **77**(1), 107 (1988)
25. Y. Hiruma, H. Nagata, T. Takenaka, *J. Appl. Phys.* **104**(12), 124106 (2008)
26. X. Tan, C. Ma, J. Frederick, S. Beckman, K.G. Webber, *J. Am. Ceram. Soc.* **94**(12), 4091 (2011)
27. C.W. Tai, S.H. Choy, H.L.W. Chan, *J. Am. Ceram. Soc.* **91**(10), 3335 (2008)
28. Y. Hiruma, H. Nagata, T. Takenaka, *Jpn. J. Appl. Phys.* **45**(9B), 7409 (2006)
29. Y. Hiruma, H. Nagata, T. Takenaka, *Jpn. J. Appl. Phys.* **48**(9S1), 09KC08 (2009)
30. P.K. Panda, *J. Mater. Sci.* **44**(19), 5049 (2009)
31. A. Hussain, J.U. Rahman, A. Zaman, R.A. Malik, J.S. Kim, T.K. Song, W.J. Kim, M.H. Kim, *Mater. Chem. Phys.* **143**(3), 1282 (2014)
32. R. Cheng, Z. Xu, R. Chu, J. Hao, J. Du, G. Li, *J. Eur. Ceram. Soc.* **36**(3), 489 (2016)
33. Y. Hiruma, Y. Imai, Y. Watanabe, H. Nagata, T. Takenaka, *Appl. Phys. Lett.* **92**(26), 262904 (2008)
34. D. Rout, K.-S. Moon, S.-J.L. Kang, I.W. Kim, *J. Appl. Phys.* **108**(8), 084102 (2010)
35. S. Sayyed, S.A. Acharya, P. Kautkar, V. Sathe, *RSC Adv.* **5**(63), 50644 (2015)
36. J.R. Gomah-Petry, A.N. Salak, P. Marchet, V.M. Ferreira, J.P. Mercurio, *Phys. Status Solidi B* **241**(8), 1949 (2004)
37. Y. Watanabe, Y. Hiruma, H. Nagata, T. Takenaka, *Ceram. Int.* **34**(4), 761 (2008)
38. M. Acosta, W. Jo, J. Rödel, *J. Am. Ceram. Soc.* **97**(6), 1937 (2014)
39. J.-H. Cho, J.-S. Park, S.-W. Kim, Y.-H. Jeong, J.-S. Yun, W.-I. Park, Y.-W. Hong, J.-H. Paik, *J. Eur. Ceram. Soc.* **37**(10), 3313 (2017)
40. J.-H. Park, H.-Y. Lee, S.-J.L. Kang, *Appl. Phys. Lett.* **104**(22), 222910 (2014)
41. S. Sheets, A. Soukhokaj, N. Ohashi, Y. Chiang, *J. Appl. Phys.* **90**(10), 5287 (2001)
42. S.R. Kanuru, K. Baskar, R. Dhanasekaran, B. Kumar, *J. Cryst. Growth* **441**, 64 (2016)
43. M. Woll, M. Burianek, D. Klimm, S. Gorfman, M. Mühlberg, *J. Cryst. Growth* **401**, 351 (2014)
44. J. Yang, Q. Yang, Y. Li, Y. Liu, *J. Eur. Ceram. Soc.* **36**(3), 541 (2016)
45. J. Bubesh Babu, M. He, D.F. Zhang, X.L. Chen, R. Dhanasekaran, *Appl. Phys. Lett.* **90**(10), 102901 (2007)
46. K.-S. Moon, D. Rout, H.-Y. Lee, S.-J.L. Kang, *J. Cryst. Growth* **317**(1), 28 (2011)
47. S.-J.L. Kang, J.-H. Park, S.-Y. Ko, H.-Y. Lee, *J. Am. Ceram. Soc.* **98**(2), 347 (2015)
48. J.G. Fisher, A. Benčan, J. Holc, M. Kosec, S. Vernay, D. Rytz, *J. Cryst. Growth* **303**(2), 487 (2007)
49. M.U. Farooq, J.G. Fisher, *Ceram. Int.* **40**(2), 3199 (2014)
50. M.U. Farooq, S.Y. Ko, J.G. Fisher, *Adv. Appl. Ceram.* **115**(2), 81 (2016)
51. D. Lee, H. Vu, H. Sun, T.L. Pham, D.T. Nguyen, J.-S. Lee, J.G. Fisher, *Ceram. Int.* **42**(16), 18894 (2016)
52. D.K. Lee, H. Vu, J.G. Fisher, *J. Electroceram.* **34**(2–3), 150 (2015)
53. J.-H. Park, S.-J.L. Kang, *AIP Adv.* **6**(1), 015310 (2016)
54. H. Sun, J.G. Fisher, S.-H. Moon, H. Tran Tran, J.-S. Lee, H.-S. Han, H.-P. Kim, W. Jo, *Mater. Sci. Eng. B* **223**, 109 (2017)
55. J. Koruza, V. Rojas, L. Molina-Luna, U. Kunz, M. Duerschnabel, H.-J. Kleebe, M. Acosta, *J. Eur. Ceram. Soc.* **36**(4), 1009 (2016)
56. S.J.L. Kang, M.G. Lee, S.M. An, *J. Am. Ceram. Soc.* **92**(7), 1464 (2009)
57. S.-J.L. Kang, S.-Y. Ko, S.-Y. Moon, *J. Ceram. Soc. Jpn.* **124**(4), 259 (2016)
58. R.D. Shannon, *Acta Crystallogr. A* **32**(5), 751 (1976)
59. T. Yang, L. Du, C. Zhai, Z. Li, Q. Zhao, Y. Luo, D. Xing, M. Zhang, *J. Alloys Compd.* **718**, 396 (2017)
60. S. Song, S. Huang, R. Zhang, Z. Chen, T. Wen, S. Wang, T. Hayat, A. Alsaedi, X. Wang, *Chem. Eng. J. (Lausanne)* **325**, 576 (2017)
61. J. Bao, X. Zhang, B. Fan, J. Zhang, M. Zhou, W. Yang, X. Hu, H. Wang, B. Pan, Y. Xie, *Angew. Chem. Int. Ed.* **54**(25), 7399 (2015)
62. P.A.W. van der Heide, Q.D. Jiang, Y.S. Kim, J.W. Rabalais, *Surf. Sci.* **473**(1), 59 (2001)
63. E. Cao, Y. Qin, T. Cui, L. Sun, W. Hao, Y. Zhang, *Ceram. Int.* **43**(10), 7922 (2017)
64. L.T. Hudson, R.L. Kurtz, S.W. Robey, D. Temple, R.L. Stockbauer, *Phys. Rev. B* **47**(16), 10832 (1993)
65. Z. Ai, G. Lu, S. Lee, *J. Alloys Compd.* **613**, 260 (2014)
66. R.E. Tanner, Y. Liang, E.I. Altman, *Surf. Sci.* **506**(3), 251 (2002)
67. A. Ito, H. Masumoto, T. Goto, *Mater. Trans.* **47**(11), 2808 (2006)
68. Y. Shi, L. Luo, Y. Zhang, Y. Chen, S. Wang, L. Li, Y. Long, F. Jiang, *Ceram. Int.* **43**(10), 7627 (2017)
69. J. Wang, W. Jiang, D. Liu, Z. Wei, Y. Zhu, *Appl. Catal. B Environ.* **176**, 306 (2015)
70. Y. Teng, F. Teng, *Electrochim. Acta* **244**, 1 (2017)
71. J. Wang, Y. Yu, L. Zhang, *Appl. Catal. B Environ.* **136**, 112 (2013)
72. Y.I. Jung, D.Y. Yoon, S.J.L. Kang, *J. Mater. Res.* **24**(9), 2949 (2009)
73. J.G. Fisher, S.-J.L. Kang, *Trans. Mater. Res. Soc. Jpn* **35**(3), 455 (2010)
74. S.-Y. Chung, D.Y. Yoon, S.-J.L. Kang, *Acta Mater.* **50**(13), 3361 (2002)
75. B.-K. Yoon, B.-A. Lee, S.-J.L. Kang, *Acta Mater.* **53**(17), 4677 (2005)
76. K.-S. Oh, J.-Y. Jun, D.-Y. Kim, N.M. Hwang, *J. Am. Ceram. Soc.* **83**(12), 3117 (2000)
77. S.-J.L. Kang, Y.-I. Jung, S.-H. Jung, J.G. Fisher, in *Microstructural Design of Advanced Engineering Materials*, ed. by D.A. Molodov (Wiley-VCH Verlag GmbH & Co. KGaA, Weinheim, 2013), p. 299
78. W. Jo, D.-Y. Kim, N.-M. Hwang, *J. Am. Ceram. Soc.* **89**(8), 2369 (2006)
79. K.W. Lay, *J. Am. Ceram. Soc.* **51**(7), 373 (1968)
80. J.P. Hirth, G.M. Pound, *Condensation and Evaporation: Nucleation and Growth Kinetics* (Pergamon Press, Oxford, 1963), pp. 77–106
81. I.V. Markov, *Crystal Growth for Beginners: Fundamentals of Nucleation, Crystal Growth and Epitaxy*, (World Scientific, Singapore, 2003), pp. 77–179
82. S.J.L. Kang, Y.I. Jung, S.H. Jung, J.G. Fisher, in *Microstructural Design of Advanced Engineering Materials*, ed. by D. A. Molodov. Interface structure-dependent grain growth behavior in polycrystals (Wiley-VCH Verlag GmbH & Co. KGaA, Weinheim, 2013), p. 299

83. S.D. Peteves, R. Abbaschian, *Metall. Trans. A.* **22**(6), 1259 (1991)
84. S.D. Peteves, R. Abbaschian, *Metall. Trans. A.* **22**(6), 1271 (1991)
85. I.V. Markov, *Crystal Growth for Beginners: Fundamentals of Nucleation, Crystal Growth and Epitaxy*, (World Scientific, Singapore, 2003), pp. 1-75
86. S.-Y. Choi, S.-J.L. Kang, *Acta Mater.* **52**(10), 2937 (2004)
87. H.J.W. Zandvliet, O. Gurlu, B. Poelsema, *Phys. Rev. B* **64**(7), 073402 (2001)
88. H. van Beijeren, *Phys. Rev. Lett.* **38**(18), 993 (1977)
89. D.-K. Lee, H. Vu, J.G. Fisher, *J. Electroceram.* **34**(2–3), 150 (2014)
90. K.L. Merkle, L.J. Thompson, *Mater. Lett.* **48**(3–4), 188 (2001)
91. S.H. Jung, S.J.L. Kang, *Scr. Mater.* **82**, 49 (2014)
92. K.-S. Moon, S.-J.L. Kang, *J. Am. Ceram. Soc.* **91**(10), 3191 (2008)
93. H. Moon, B.-K. Kim, S.-J.L. Kang, *Acta Mater.* **49**(7), 1293 (2001)
94. C. Rottman, M. Wortis, *Phys. Rev. B* **29**(1), 328 (1984)
95. C. Rottman, M. Wortis, *Phys. Rep.* **103**(1–4), 59 (1984)
96. K. Choi, N.M. Hwang, D.-Y. Kim, *J. Am. Ceram. Soc.* **85**(9), 2313 (2002)
97. W. Jo, N.-M. Hwang, D.-Y. Kim, *J. Korean Ceram. Soc.* **43**(11), 728 (2006)
98. K.-S. Moon, D. Rout, H.-Y. Lee, S.-J.L. Kang, *J. Eur. Ceram. Soc.* **31**(10), 1915 (2011)
99. U.C. Oh, Y.S. Chung, D.Y. Kim, D.N. Yoon, *J. Am. Ceram. Soc.* **71**(10), 854 (1988)
100. D. Jenko, A. Bencan, B. Malic, J. Holc, M. Kosec, *Microsc. Microanal.* **11**(6), 572 (2005)
101. J.G. Fisher, A. Bencan, M. Kosec, S. Vernay, D. Rytz, *J. Am. Ceram. Soc.* **91**(5), 1503 (2008)
102. S.-Y. Ko, S.-J.L. Kang, *J. Eur. Ceram. Soc.* **36**(5), 1159 (2016)
103. J.G. Fisher, S.-J.L. Kang, *J. Eur. Ceram. Soc.* **29**(12), 2581 (2009)
104. Y.S. Sung, J.M. Kim, J.H. Cho, T.K. Song, M.H. Kim, T.G. Park, *Appl. Phys. Lett.* **98**(1), 012902 (2011)
105. Y.S. Sung, J.M. Kim, J.H. Cho, T.K. Song, M.H. Kim, H.H. Chong, T.G. Park, D. Do, S.S. Kim, *Appl. Phys. Lett.* **96**(2), 022901 (2010)